Stable interstitial layer to alleviate fatigue fracture of high nickel cathode for lithium-ion batteries

Chengkai Yang[a,1], Ruiwen Shao[b,1], Yingying Mi[a], Lanyao Shen[d], Binglu Zhao[a], Qian wang[a], Kai Wu[a], Wen Lui[c,**], Peng Gao[b,e,***], Henghui Zhou[a,*]

[a] College of Chemistry and Molecular Engineering, Peking University, 100871, Beijing, China
[b] Electron Microscopy Laboratory, School of Physics, Peking University, 100871, Beijing, China
[c] College of Science, Beijing University of Chemical Technology, 100092, Beijing, China
[d] China Beijing Engineering Research Center of Power Lithium-ion Battery, 102202, Beijing, China
[e] Collaborative Innovation Center of Quantum Matter, 100871, Beijing, China

HIGHLIGHTS

- The high-Ni cathode was treated by an interstitial coating without capacity loss.
- The interstitial layer imparts high capacity retention of 88.5% after 200 cycles.
- The coated particles show structure integrity other than cracking.
- The morphology degradation is a fatigue process within long-term cycling.
- The coated cathode has an excellent elastic recovery leading to long cycle life.

GRAPHICAL ABSTRACT
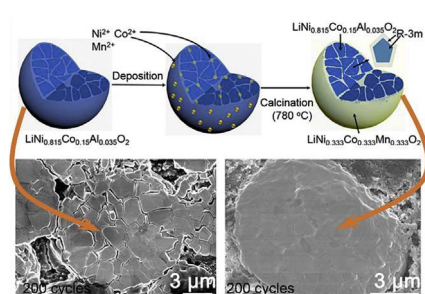
ARTICLE INFO

ABSTRACT

High nickel cathodes can deliver higher capacity with lower cost than conventional $LiCoO_2$, however, the irreversible structural and morphology degradation with long-term cycling hinder their further application. In this paper, $LiNi_{0.815}Co_{0.15}Al_{0.035}O_2$ agglomerates are treated by $LiNi_{0.333}Co_{0.333}Mn_{0.333}O_2$ coating to get a stable interstitial layer without capacity loss. The interstitial layer is about 10 nm in thickness and has a layered (R-3m) structure, which can improve the chemical and mechanical stability of cathode materials with capacity retention of 88.5% after 200 cycles. The structural analysis and in-situ compression test proves that the morphology degradation is a fatigue process within long-term electrochemical reaction, and the coated sample has an excellent elastic recovery capacity thus leading to long cycle life.

1. Introduction

With the expansion of hybrid electric vehicles (HEVs) and electric vehicles (EVs), the next generation lithium-ion batteries (LIB) demand cathode materials with higher capacities and better cycling stability [1]. Developing prominent cathodes with high energy density and high

power density has been raised and carried out by many researchers. High-Nickel cathodes, such as $LiNi_{0.8}Co_{0.1}Mn_{0.1}O_2$ [2], Li-$Ni_{0.815}Co_{0.15}Al_{0.035}O_2$ [3] are considered as promising candidates to meet the increasing energy density requirements due to their high specific capacity and high power density [4].

However, the main challenges for the high nickel cathodes still exist on the drastic structural degradation and poor cycling performance caused by the repeating lattice change during lithiation/delithiation and harmful side reactions on the surface [5]. Tremendous attempts have been conducted to eliminate above issues [6–8]. The well-designed ion doping and surface-coating strategies have been reported intensively, however, little emphasis has been put on reducing the inner stress of cathode material caused by phase transition with lithium intercalation/deintercalation [9].

In our previous work, we have carried out a systematic investigation on the inner structure of the high nickel cathode material, and found that the secondary structures (i.e. the arrangement of primary particles) had great influence on the physical and electrochemical properties, such as sintering property, rate performance and cycle life [10]. During charging and discharging, internal stress in cathode material is generated because of the interaction of lithium ions with the lattice structure. The stresses induced by the electrochemical reaction may cause irreversible damage to the secondary structure and accelerate side reactions with the increasing surface area owing to the formation of cracks [1,11]. Although there are some methods reported to address the morphological degradation, the influence of *in-situ* stress on cathode materials is not studied yet.

Here, we modified the surface of $LiNi_{0.815}Co_{0.15}Al_{0.035}O_2$ (abbreviated as NCA) agglomerates by forming a stable layer of $LiNi_{0.333}Co_{0.333}Mn_{0.333}O_2$ (NCM333) as interstitial coating without capacity loss. The design strategy is multifold: First, the interstitial layer has higher content of Mn and Co than that in the bulk thus can provide more stable surface towards electrolyte. Secondly, the lattice matching between the interstitial layer and bulk material can lease the boundary stress. Third, unlike surface coating, the interstitial layer could protect the inner primary particles other than merely the outer surface of the secondary particle. The electrochemical performances of the hybrid cathode materials would be improved due to the formation of a stable interstitial layer. Stable cycling performance is demonstrated for 200 cycles with the capacity retention of 88.5%. The coated sample also show superior storage performance compared to the bare NCA cathode. In addition, we combined *in-situ* stress measurement and electrochemical test to reveal the underlying mechanism of the morphological degradation and further demonstrated the superiority of the interstitial coating.

2. Experimental

2.1. Synthesis of NCA and NCA-NCM cathode materials

The spherical precursor $Ni_{0.815}Co_{0.15}Al_{0.035}(OH)_2$ was synthesized by a modified co-precipitation method [1]. Briefly, proper amounts of $NiSO_4$, $CoSO_4$ and $AlSO_4$ (cationic ratio of Ni: Co: Mn = 815:150:35) were added to a strongly stirred tank reactor under nitrogen atmosphere, forming a 2.0 mol L^{-1} solution. A 2.0 mol L^{-1} ammonia as a complexation agent and a 4.0 mol L^{-1} NaOH solution as precipitate agent were also pumped into the reactor at the same time. The obtained precursor was then dried at 120 °C for 4 h in the air. After drying, the precursor and $LiOH·H_2O$ were ball milled for 4 h to make uniform mixture. The Li/TM molar ratio of mixture was fixed at 1.05 [12,13]. The mixture was heated to 550 °C at a heating rate of 5 °C/min, then heated to 780 °C at a heating rate of 10 °C/min and finally calcined for 10 h in the O_2. The NCA-NCM sample was prepared in a 40 ml ethanol solution of 2 wt % $(CH_3COO)_2Co$, $(CH_3COO)_2Mn$, and $(CH_3COO)_2Ni$. 10 g of the NCA cathode was added to the solution. The mixed solution was stirred at 60 °C until the solvent completely evaporated. The surface treated samples were then calcinated at 780 °C for 5 h in O_2.

2.2. Materials characterization

The sample structures were identified by powder X-ray diffraction (XRD, Cu Kα radiation, Bruker D8 Advance). X-ray photoelectron spectroscopy (XPS, Kratos Analytical Ltd., Axis Ultra) was performed to compare the valence state of the elements. The peak fitting of Ni 2p was based on following guidelines: the area ratio of Ni 2p $_{3/2}$ to Ni 2p $_{1/2}$ was constraint at 2:1; the half-peak width was constraint the same for a pair of peaks. The morphology and element distribution were analyzed using scanning electron microscope (SEM, Hitachi S-4800) equipped with an energy dispersive spectrometer (EDS, Horiba, EX-250) and a field-emission high resolution transmission electron microscope (HRTEM, JEM-2100F). The cross-sectional SEM samples were prepared by a low-energy Ar-ion milling system (Gatan Model 691PIPS).

2.3. Electrochemical tests

The working electrode was prepared by mixing active material (90 wt%), carbon black conductive additive (Super P, 5 wt%), and polyvinylidenefluoride binder (PVDF, 5 wt%) dissolved in N-methyl-pyrrolidone (NMP). The slurry was then casted on aluminum foil and followed by drying at 120 °C for 24 h in vacuum oven. Electrolyte was a mixture of ethylene carbonate (EC), ethyl methyl carbonate (EMC), and dimethyl carbonate (DMC) containing lithium hexafluorophosphate ($LiPF_6$). Celgard 2400 film was used as the separator. The cells were assembled in an argon-filled glove box with H_2O and O_2 concentrations below 0.01 ppm. All the electrochemical performance was performed on a LAND CT2001C battery test system (Wuhan, China) between 2.8 and 4.25 V at different charge/discharge rates (1 C = 160 mA g^{-1}) at 25 °C. Cyclic voltammetry (CV) tests of the bare and coated samples were conducted in the voltage range of 2.8–4.3 V with a scan rate of 0.1 mV s^{-1}.

Electrochemical impedance spectroscopy (EIS) was measured in the frequency range from 10^5 to 10^{-2} Hz with an amplitude of 5 mV (CHI660E, Shanghai, China). Before EIS measurements, the cells were equilibrated at the charge state of 4.25 V after three cycles (0.1 C/ 0.1 C).

3. Results and discussion

3.1. Synthesis of the interstitial coated high nickel cathode (NCA-NCM)

The schematic illustration in Fig. 1a shows the fabrication process for the interstitial coating on $LiNi_{0.815}Co_{0.15}Al_{0.035}O_2$ with Li-$Ni_{0.333}Co_{0.333}Mn_{0.333}O_2$ layer (the coated materials abbreviated as NCA-NCM). The interstitial coating treatment was started with cobalt, manganese and nickel acetate completely dissolved in solvent, and percolated along the grain boundaries into the secondary particles. Then, the coating precursor gradually deposited on the surface and inside the particle because of acetates hydrolysis and solvent evaporation [14]. The modification method is simple and facile, which can be easily scale up and used for practical application.

Fig. 1b–j illustrate the morphology change of the NCA-NCM secondary particles during the coating process. Before coating, the NCA sample has a smooth outer surface on the particle (Fig. 1b), and round shaped grains inside the particle (Fig. 1c). Thereafter, plenty of nanoparticles can be observed on the surface of NCA grains after being coated with $Ni_{0.333}Co_{0.333}Mn_{0.333}(OH)_2$. The surface roughness of the prepared NCA-NCM decreases significantly after annealing, indicating that the NCM333 nanoparticles were fused with the NCA grains. Unlike surface metal oxides coating in other works [1,14,15], calcination at high temperature of 780 °C in our work without additional lithium salt can still form an R-3m phase NCM333 coating layer with no capacity loss.
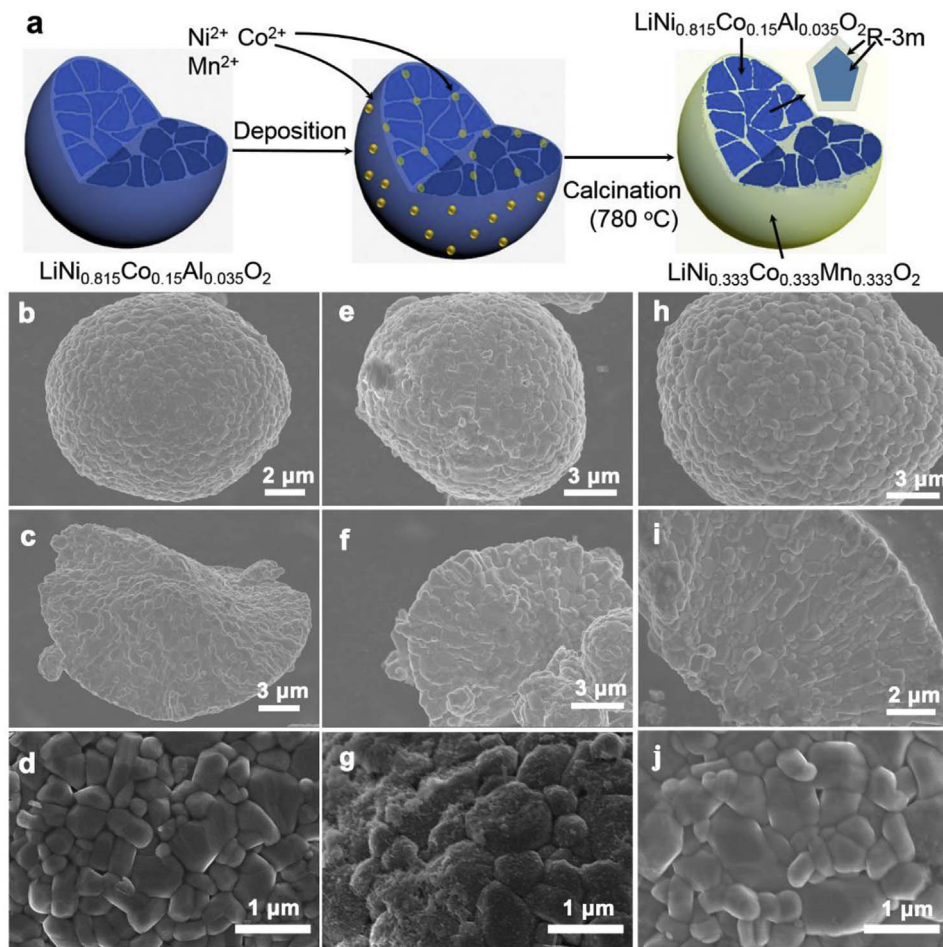
Fig. 1. The synthesis scheme of NCA-NCM with interstitial layer and morphology characterization of NCA, NCA-NCM before and after sintering. (a) Schematic illustration of the interstitial coating. SEM images of (b–d) NCA, (e–g) NCA-NCM before sintering, and (h–j) NCA-NCM after sintering.
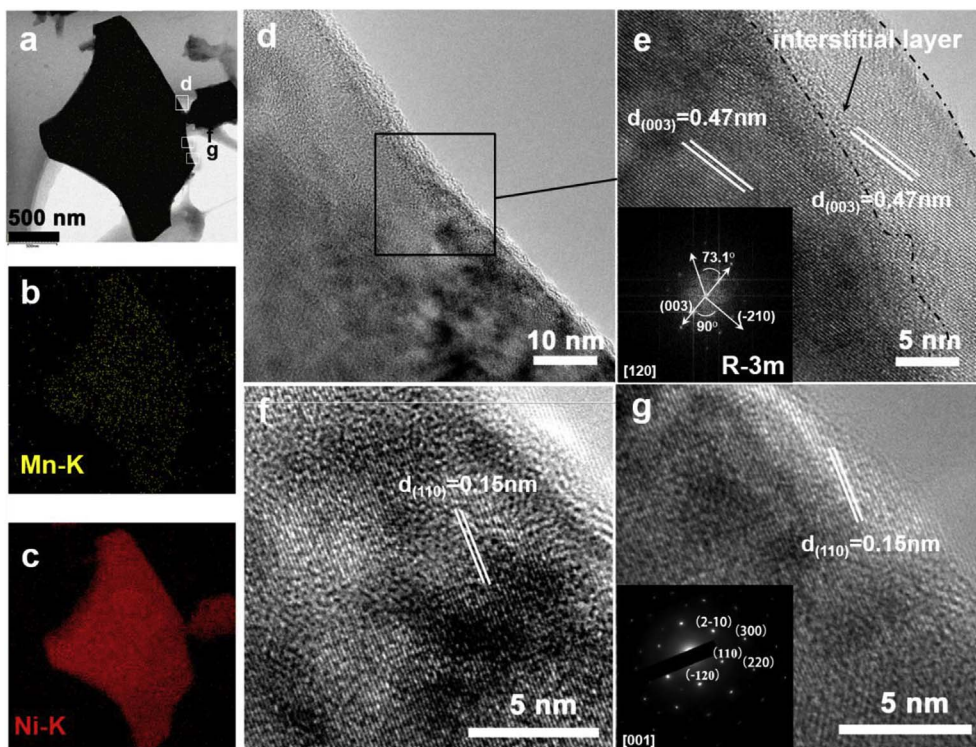
Fig. 2. Characterization of the interstitial coated NCA-NCM. (a)TEM image of NCA-NCM and the corresponding EDS elemental mapping of (b) Mn and (c) Ni. (d, f, g) TEM images of NCA-NCM surface regions selected in (a). (e) Zoom image of the selected area in (d). The insets in e and g show the corresponding FFT and SAED patterns.
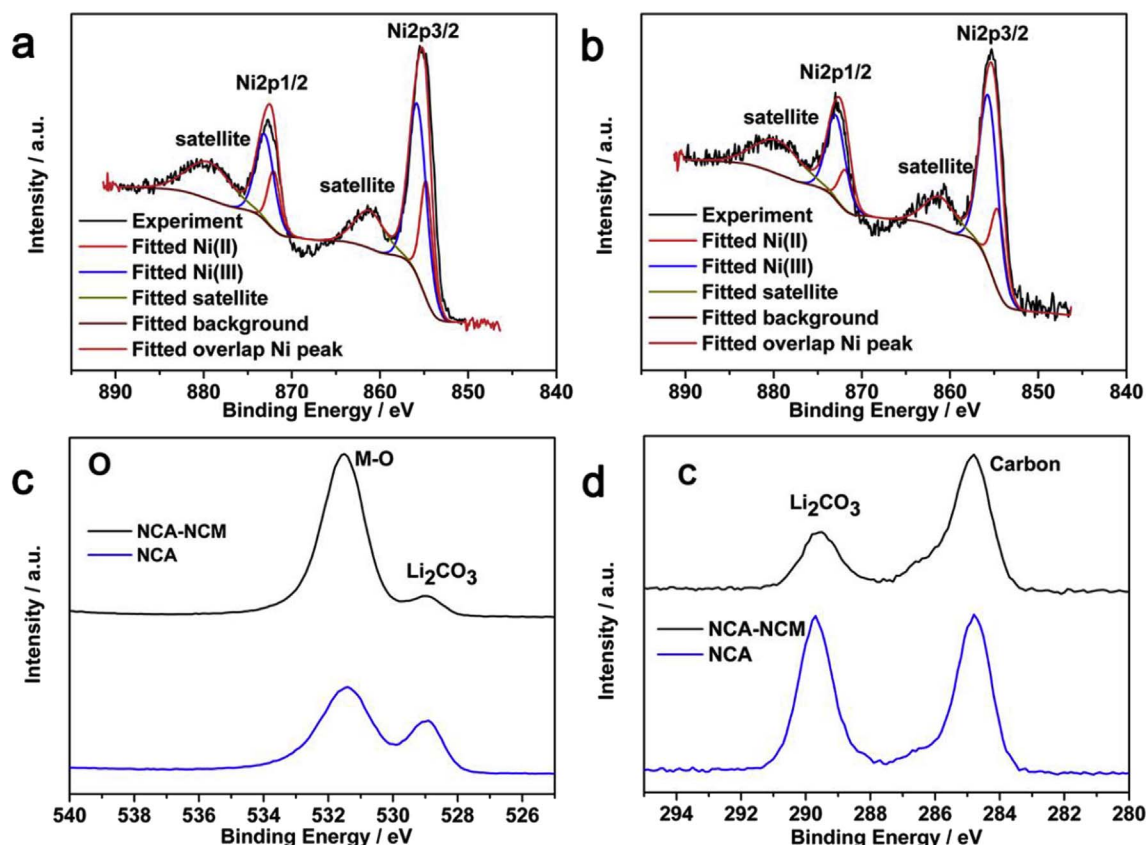
Fig. 3. XPS analysis of NCA and NCA-NCM. Ni2p core level spectra of (a) NCA-NCM and (b) NCA. (c) O1s and (d) C1s XPS of HNC and NCA-NCM.

TEM and EDS mapping are conducted to give more detailed structure and surface information of the two samples (Fig. 2). The distribution of Mn is uniform throughout the whole particles in Fig. 2b, indicating the perfect percolation of precursors into the NCA aggregates during the coating process. The selected areas in Fig. 2a are enlarged as Fig. 2d, f, g. Clear surface interstitial layer can be noticed in TEM of Fig. 2d and HRTEM images of Fig. 2e. The typical lattice fringes of 0.47 nm in Fig. 3e confirm the well-established R-3m space group of the NCM333 interstitial layer [5,16,17]. The interstitial layer has very similar crystal structure with the bulk, indicating that the interstitial layer could also intercalate and deintercalate of lithium and have no negative effect on the performance of bulk materials. The Fast Fourier Transform (FFT) analysis (inset of Fig. 2e) further provides characteristics of the layered structure. In consideration of the anisotropically oriented crystal particles in Ni-rich materials, there are other growth directions observed as shown in Fig. 2f, g. The lattice fringes of 0.15 nm and inset in Fig. 2g verify the R-3m space group in Ni-rich material with the incidence electrons along [001] direction [18]. In the anisotropically oriented crystal particles, the coating layers still have the same structure with bulk materials. In addition, the crystal structure after cycling as determined from HRTEM (Supplementary Materials, Figs. S6 and S7) demonstrates the chemical stability of coated NCA-NCM samples.

3.2. Surface analysis of the interstitial coated sample

The content of residual lithium is an important parameter for cathode material design [19]. Thus the amounts of residual lithium of NCA before and after interstitial coating were measured using Stepwise Titration of polyacidic base, and the results were listed in Table S1 (supporting information). For the NCA-NCM cathodes, the total residual lithium is 0.586 wt%, which is much lower than that of the bare NCA cathodes (2.46 wt %). The decrease of residual lithium on the NCA-

NCM is a result of the reactions between $Ni_{0.333}Co_{0.333}Mn_{0.333}O_{1+x}(OH)_2$ and LiOH at high-temperature forming $LiNi_{0.333}Co_{0.333}Mn_{0.333}O_2$ interstitial layer, which can also deliver capacity because of its R-3m space group [20].

Chemical state of Ni, C, and O were explored by X-ray photoelectron spectroscopy (XPS) in Fig. 3. The binding energy of Ni^{3+} $2p_{3/2}$, Ni^{2+} $2p_{3/2}$ of the NCA sample at 855.6 eV, 854.6 eV are similar with the references reported for Ni in $LiMO_2$ (M represents transition metals) [19,21–23]. As for NCA-NCM materials, there is no remarkable chemical shift for binding energy of Ni $2p_{3/2}$ after the coating process. The ratio of Ni^{3+} $2p_{3/2}$ to Ni^{2+} $2p_{3/2}$ for NCA and NCA-NCM are 2.90 and 2.23, respectively. It indicates that the content of Ni^{2+} at the surface region ascends after being coated with NCM333 as the valence state of Ni ion is +2 in NCM333 and +3 in $LiNiO_2$. The O 1s spectra can be divided into two peaks at 529.0 and 531.5 eV in Fig. 3c, which are associated with the metal-oxygen bonding and the residual oxygen containing lithium impurities such as Li_2CO_3, respectively. Compared with the bare NCA materials, the content of residual lithium impurities in the NCA-NCM materials decrease due to the coating process, which can be further confirmed by the same trend for Li_2CO_3 in C 1s XPS in Fig. 3d. The interstitial coating can reduce the average oxidation state of Ni and also decrease the content of residual lithium impurities, which is also in consistence with the titration results.

3.3. The electrochemical performance

The electrochemical behavior of the bare (NCA) and interstitial coated sample (NCA-NCM) were first studied by Cyclic Voltammetry (CV) at a scan rate of 0.1 mV s^{-1}, as presented in Figs. S3 and S4. In general, the peaks of the CV curves match well with the redox reactions caused by lithium insertion and extraction (Fig. S3). In the first delithiation step, only two oxidation peaks can be observed which corresponding to the Ni^{3+} to Ni^{4+} and Co^{3+} to Co^{4+}. In the following
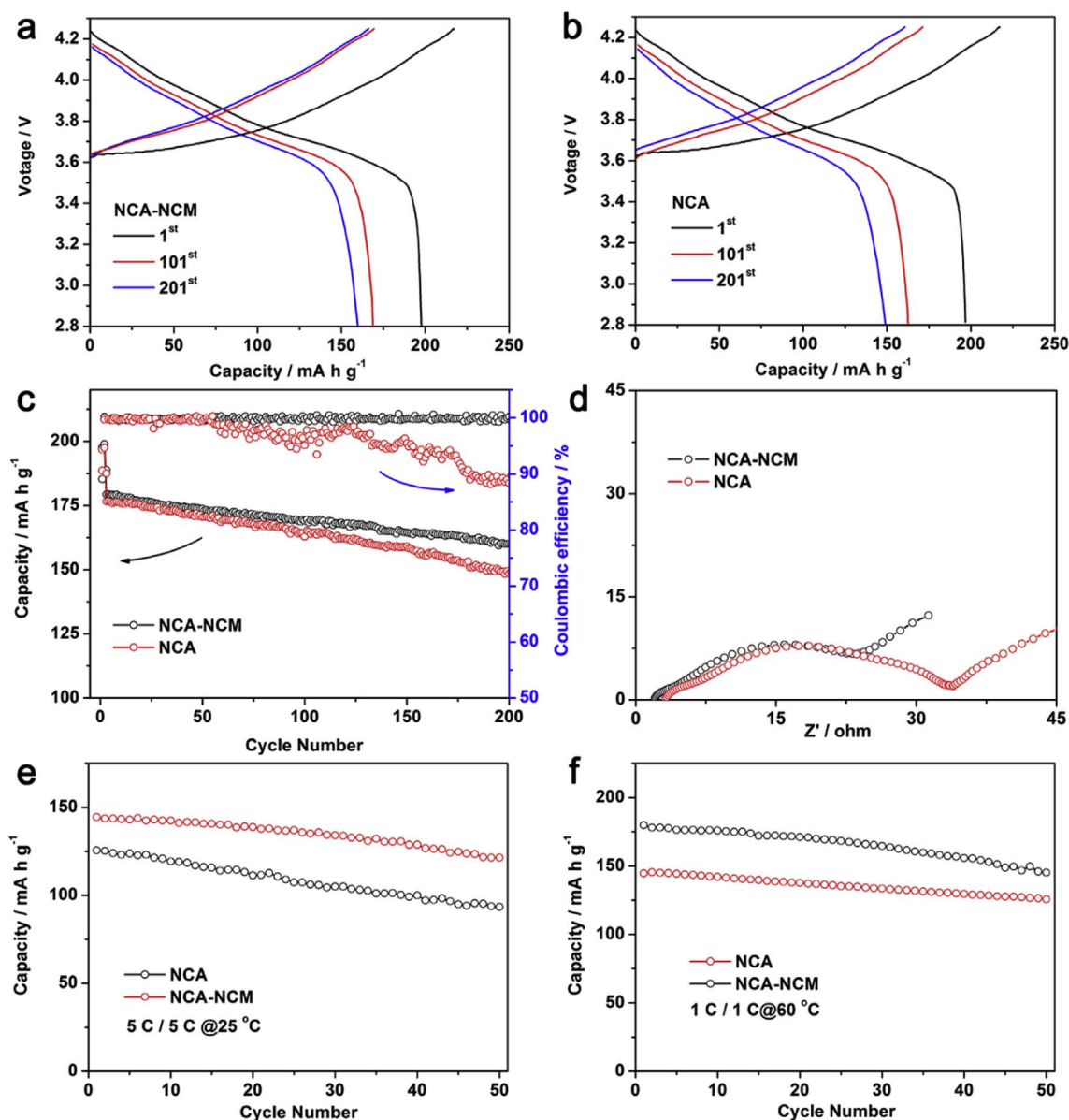
Fig. 4. Electrochemical performance of the NCA and NCA-NCM cathodes. Charge/discharge profiles of the (a) NCA-NCM and (b) NCA cathodes. (c) Cycle performance of the NCA and NCA-NCM cathodes between 2.8 and 4.25 V at 25 °C (charging at 0.5 C and discharging at 1 C). (d) EIS spectra of the NCA and NCA-NCM cathodes. (e) Rate capabilities of NCA-NCM and NCA samples stored for three months in dry air evaluated between 2.8 and 4.25 V at 5 C at 25 °C. (f) Cycle performance of the NCA-NCM and NCA samples stored for three months in dry air between 2.8 and 4.25 V at 1 C at 60 °C.

cycles, three main peaks in the oxidation curves can be observed, which were attributed to the phase transformation from hexagonal to monoclinic (H1 to M), monoclinic to hexagonal (M to H2) and hexagonal to hexagonal (H2 to H3), and vice versa in the reduction curves [24]. In addition, the shape of CV curves after interstitial coating is similar to the bare NCA sample, which indicates that the coating process doesn't interfere with the redox mechanism.

The capacity and cycle stability of the NCA and NCA-NCM cathodes were examined on a LAND CT2001C. Fig. 4a, b presents the typical initial charge-discharge profiles of NCA-NCM and NCA in the voltage range of 2.8–4.25 V at 25 °C. The charge and discharge rate was 0.1 C for the 1st-2nd cycle; In the 3rd-202th cycle, the cells charged at 0.5 C and discharged at 1.0 C. The 1st charge-discharge profile of the NCA-NCM shows no capacity loss compare to the NCA cathode even after a large dose of interstitial material coated on it. The NCA sample delivers initial charge and discharge capacities of 217.3 and 196.8 mA h g^{-1} with a coulombic efficiency of 90.6%. And the NCA-NCM sample delivers initial charge and discharge capacities of 221.8 and

197.6 mA h g^{-1} with a coulombic efficiency of 89.1%, indicating that there is almost no difference between two samples at the first cycle. However, after 200 cycles, the capacity of NCA-NCM is 10.7 mA h g^{-1} higher than that of NCA. The cycling performance of two samples is compared in Fig. 4c. The interstitial coated NCA-NCM cathode presents an excellent long-term cycling performance, which retains about 88.5% of the initial capacity after 200 cycles. In contrast, the capacity retention of NCA is only 84.7%. Moreover, the coulombic efficiency of NCA sample declines sharply after about 60 cycles, indicating the occurrence of morphology deterioration and fracture, which create more surfaces that are unstable and lead to more side reactions. In addition, the store properties of cathode materials were studied after storing in ambient condition for 3 months. The NCA-NCM sample exhibits better rate performance and high temperature performance than the NCA sample (Fig. 4e and f). The discharge capacities are 179.8 mA h g^{-1} at 1 C under 60 °C and 144.4 mA h g^{-1} at 5 C under 25 °C for the coated samples, which are much higher than that of the bare samples with 144.6 and 126.6 mA h g^{-1}, respectively. The huge difference in store

performance is related to the surface chemical stability and the residual lithium content [19,21]. The high-nickel layered materials exhibit unstable surface structure and vulnerable to the humidity and CO_2 in air. After coating, the sample is more robust in resisting the H_2O and CO_2 of environment, which strengthen the structure stability.

Extended electrochemical tests of the two samples were further carried out by Electrochemical Impedance Spectroscopy (EIS) analysis (Fig. 4d). The EIS spectra consists of high-frequency semi-circles, intermediate-frequency semi-circles, and low frequency inclined lines. The high-frequency semi-circles refer to the resistance for Li^+ ion migration through the surface film (R_f) and film capacitance; while the second intermediate semi-circles correspond to charge transfer resistance (R_{ct}) and the capacity between the electrode and electrolyte interface; the low-frequency inclined lines represent the Li^+ ion diffusion in bulk materials [25,26]. The resistance values of the two samples obtained from EIS fitting are presented in Table S2. The smaller R_{ct} of NCA-NCM (25.8 Ω) than that of NCA (29.2 Ω) demonstrates the faster Li^+ ion intercalation rate of NCA-NCM. Therefore, the interstitial layer composed of NCM333 can provide fast pathways for Li^+ ion intercalation with a lower charge transfer resistance.

3.4. Postmortem SEM analysis

The cross-sectional SEM images of the NCA and NCA-NCM secondary particles after 200 cycles between 2.8 and 4.25 V are shown in Fig. 5. The fragmentation of the secondary particles is observed obviously after cycling. Serious cracks and grain boundaries occur due to the repeated volume change of the high-nickel unit cell during Li^+ intercalation and deintercalation [27]. On the contrast, NCA-NCM particles show integral morphology without noticeable cracks even after 200 cycles, confirming that the NCM333 interstitial layer could effectively connect the adjacent grains and ease the inner stress during charge and discharge. Interestingly, the micro-cracks are almost distributed on the grain boundary instead of grain interior, that the stress from Li^+ ion migration is too weak to destroy the single crystal grains. There are two possible reasons could account for the interstitial coating effect. One is that the NCM333 layers enhance the binding strength of primary grains in the secondary particles. The other is that the NCM333 layer reduce the volume change of the high nickel unit cell of NCA. Obviously, it is difficult to influence the volume change of NCA unit cell with merely the thin coating layer alone. In this regard, we consider the former is more credible as the interstitial coating of NCM333 can effectively glue the NCA grains together and alleviate the inner stress generated during long term cycling. As shown in the HRTEM images (Figs. S6 and 7), the layered structure of NCA-NCM was well maintained with only very thin deterioration area at the surface. However,

Fig. 5. Particle morphology of secondary particles after 200 cycles between 2.8 and 4.25 V. Cross-sectional FIB-SEM images of (a, c) NCA and (b, d) NCA-NCM particles.

extended deterioration and Rock-salt phase can be observed in the uncoated NCA samples. The amorphous deterioration region in the image of NCA samples is much larger than that of the NCA-NCM. Therefore, the interstitial coating can not only alleviate the inner stress to avoid particle cracking but also protect the inner surface of the material crystalline.

3.5. In-situ stress measurement

To get more precise information on grain crushing, the SEM image of a cracked NCA particle was processed and shown in Fig. S1. The ratio of volume change from SEM is 7.69 vol%, which is similar to the value of 5.14 vol% from XRD analysis in Fig. S2. The volume change data came from our group (supporting information, Table S3 and Fig. S2) and the K. Ishidzu et al.'s article (Fig. S3) via XRD refinement, which indicate that the volume change for NCA materials is around 5 vol% [28]. In any case, the 7.69 vol% or 5.14 vol% volume change is too small to crush the NCA crystal grain in one cycle [29]. It is thus quite difficult to observe morphology change after several cycles. Therefore, the morphology degradation and micro-cracks should originate from a mechanical fatigue process after long time cycling [30].

In-situ stress experiment on single particle was carried out to examine the mechanical property of NCA and NCA-NCM (Fig. 6). Particles with diameter of about 8 μm were selected as typical samples to go through the measurement. Several yield points (pointed by arrows in Fig. 6) can be observed on the stress-depth curve of NCA, which might be caused by glide of the grain boundary under stress. After pressing, the grains of NCA cathode are elongated along the axis of deformation [31]. It indicates that the morphology degradation raises structure degradation under stress. During repeated charging and discharging, the occurrence of fragmentation happens due to the inner stress just like the *in-situ* compression test, which leads to the capacity loss of cathodes. Meanwhile, side reactions occur on the exposed surfaces at the grain boundaries, which deteriorate the capacity loss with morphology degradation [32]. In contrast, the stress-depth curve of NCA-NCM particle fit linear relation well and there exists small hysteresis loop area, revealing the excellent elastic recovery capacity of NCA-NCM. The pristine NCA samples are more prone to crushing under stress. On the contrary, there are few cracks in the NCA-NCM samples due to the interstitial layer. Therefore, the NCM333 layer on the surface and between the grains can effectively connect the adjacent grains and improve the tensile strength or elastic recovery ability, leading to much improved stability in long-term cycling.

4. Conclusion

In summary, an interstitial coating method was introduced to improve the mechanical and electrochemical properties of the high nickel cathode $LiNi_{0.815}Co_{0.15}Al_{0.035}O_2$. After interstitial coating of $LiNi_{0.333}Co_{0.333}Mn_{0.333}O_2$, cycling performance of the cathode is largely improved and polarization significantly decreases compared to the bare ones. Cross-sectional SEM analysis shows particle breakage of $LiNi_{0.815}Co_{0.15}Al_{0.035}O_2$, which attributing to the stress generated in the charging/discharging process. The mechanism of grain crushing in the secondary particles is further revealed by *in-situ* compression test as a fatigue process within long-term electrochemical reactions, and the coated sample has an excellent elastic recovery capacity. According to results, the $LiNi_{0.815}Co_{0.15}Al_{0.035}O_2$ with interstitial coating layer can ensure lower residual lithium content and a stronger binding force between adjacent grains leading to improved long-term cycling stability. This work demonstrates that the interstitial coating strategy is effective to address the inner stress of high-Ni cathode during cycling and enlightens materials design for other cathode or anode involving volume change and stress in batteries.
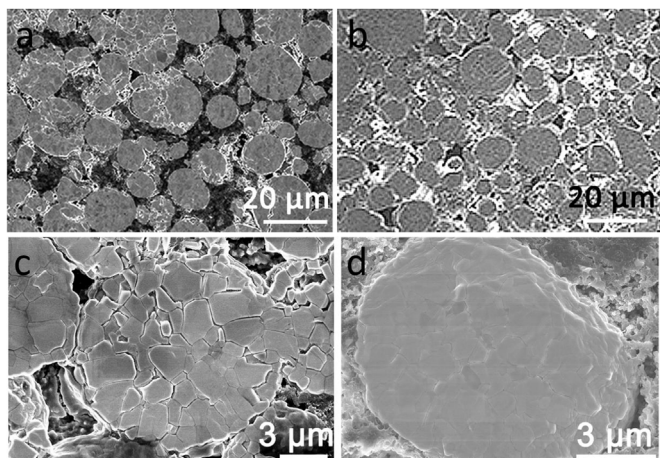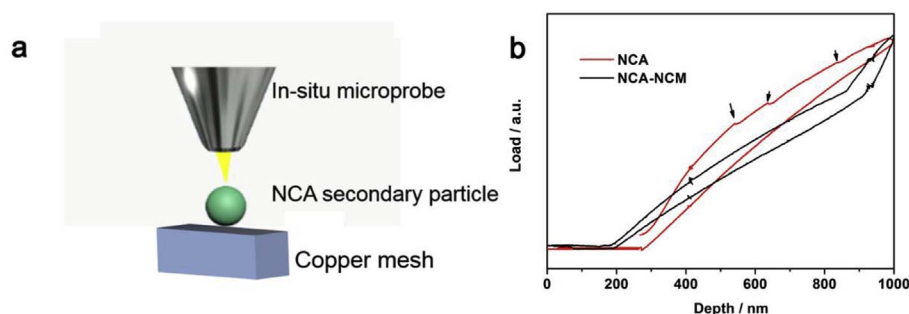
Fig. 6. (a) The scheme of *in-situ* compression test. (b) *In-situ* stress-depth curves for single particle of NCA and NCA-NCM. The arrows show several yield points.

Appendix A. Supplementary data

Supplementary data related to this article can be found at http://dx. doi.org/10.1016/j.jpowsour.2017.11.085.

References

[1] H. Kim, S. Lee, H. Cho, J. Kim, J. Lee, S. Park, S.H. Joo, S.H. Kim, Y.G. Cho, H.K. Song, S.K. Kwak, J. Cho, Adv. Mater. 28 (2016) 4705–4712.
[2] D. Andre, S.-J. Kim, P. Lamp, S.F. Lux, F. Maglia, O. Paschos, B. Stiaszny, J. Mater. Chem. A 3 (2015) 6709–6732.
[3] Y. Makimura, T. Sasaki, T. Nonaka, Y.F. Nishimura, T. Uyama, C. Okuda, Y. Itou, Y. Takeuchi, J. Mater. Chem. A 4 (2016) 8350–8358.
[4] W. Liu, P. Oh, X. Liu, M.-J. Lee, W. Cho, S. Chae, Y. Kim, J. Cho, Angew. Chem. Int. Ed. 54 (2015) 4440–4457.
[5] J. Zhao, W. Zhang, A. Huq, S.T. Misture, B. Zhang, S. Guo, L. Wu, Y. Zhu, Z. Chen, K. Amine, F. Pan, J. Bai, F. Wang, Adv. Energy Mater. 7 (2016) 1601266.
[6] S.H. Yun, K.-S. Park, Y.J. Park, J. Power Sources 195 (2010) 6108–6115.
[7] X. Feng, J. Zhang, L. Yin, Mater. Res. Bull. 74 (2016) 421–424.
[8] S.M. Lee, S.H. Oh, J.P. Ahn, W.I. Cho, H. Jang, J. Power Sources 159 (2006) 1334–1339.
[9] M. Kerlau, M. Marcinek, V. Srinivasan, R.M. Kostecki, Electrochim. Acta 52 (2007) 5422–5429.
[10] C.-K. Yang, L.-Y. Qi, Z. Zuo, R.-N. Wang, M. Ye, J. Lu, H.-H. Zhou, J. Power Sources 331 (2016) 487–494.
[11] H.F. Wang, Y.I. Jang, B.Y. Huang, D.R. Sadoway, Y.T. Chiang, J. Electrochem. Soc. 146 (1999) 473–480.
[12] M.M. Thackeray, S.-H. Kang, C.S. Johnson, J.T. Vaughey, R. Benedek, S.A. Hackney, J. Mater. Chem. 17 (2007) 3112–3125.
[13] M.M. Thackeray, C. Wolverton, E.D. Isaacs, Energy Environ. Sci. 5 (2012) 7854–7863.
[14] H. Kim, M.G. Kim, H.Y. Jeong, H. Nam, J. Cho, Nano Lett. 15 (2015) 2111–2119.
[15] Y. Cho, P. Oh, J. Cho, Nano Lett. 13 (2013) 1145–1152.
[16] S. Hwang, W. Chang, S.M. Kim, D. Su, D.H. Kim, J.Y. Lee, K.Y. Chung, E.A. Stach, Chem. Mater 26 (2014) 1084–1092.
[17] L. Li, Q. Yao, H. Zhu, Z. Chen, L. Song, J. Duan, J. Alloys Compd. 686 (2016) 30–37.
[18] G. Tan, F. Wu, J. Lu, R. Chen, L. Li, K. Amine, Nanoscale 6 (2014) 10611–10622.
[19] S. Liu, C. Zhang, Q. Su, L. Li, J. Su, T. Huang, Y. Chen, A. Yu, Electrochim. Acta 224 (2017) 171–177.
[20] L. Riekehr, J. Liu, B. Schwarz, F. Sigel, I. Kerkamm, Y. Xia, H. Ehrenberg, J. Power Sources 306 (2016) 135–147.
[21] X. Zheng, X. Li, Z. Wang, H. Guo, Z. Huang, G. Yan, D. Wang, Electrochim. Acta 191 (2016) 832–840.
[22] S. Liu, H. Wu, L. Huang, M. Xiang, H. Liu, Y. Zhang, J. Alloys Compd. 674 (2016) 447–454.
[23] R. Zhao, Z. Yang, J. Liang, D. Lu, C. Liang, X. Guan, A. Gao, H. Chen, J. Alloys Compd. 689 (2016) 318–325.
[24] M.D. Levi, K. Gamolsky, D. Aurbach, U. Heider, R. Oesten, Electrochimica Acta 45 (2000) 1781–1789.
[25] N.-S. Choi, Z. Chen, S.A. Freunberger, X. Ji, Y.-K. Sun, K. Amine, G. Yushin, L.F. Nazar, J. Cho, P.G. Bruce, Angew. Chem. Int. Ed. 51 (2012) 9994–10024.
[26] Z. Wang, Y. Zhang, B. Chen, C. Lu, J. Solid State Electrochem. 18 (2014) 1757–1762.
[27] L. Wu, X. Xiao, Y. Wen, J. Zhang, J. Power Sources 336 (2016) 8–18.
[28] K. Ishidzu, Y. Oka, T. Nakamura, Solid State Ion. 288 (2016) 176–179.
[29] C. Zhang, J. Xu, L. Cao, Z. Wu, S. Santhanagopalan, J. Power Sources 357 (2017) 126–137.
[30] S. Han, J. Park, W. Lu, A.M. Sastry, J. Power Sources 240 (2013) 155–167.
[31] H. Liu, M. Wolf, K. Karki, Y.-S. Yu, E.A. Stach, J. Cabana, K.W. Chapman, P.J. Chupas, Nano Lett. 6 (2017) 3452–3457.
[32] M. Börner, F. Horsthemke, F. Kollmer, S. Haseloff, A. Friesen, P. Niehoff, S. Nowak, M. Winter, F.M. Schappacher, J. Power Sources 335 (2016) 45–55.